Cellulose (2024) 31:8067–8086
https://doi.org/10.1007/s10570-024-06113-2

ORIGINAL RESEARCH

Lecithin/graphite modified kapok fibers for functional xerogel composites

Daiana M. F. Sandrini · Marina F. Pillis · Olandir V. Correa · Priyanka Madesh · Balaji Krishnasamy · Denise F. S. Petri

Received: 20 April 2024 / Accepted: 6 August 2024 / Published online: 12 August 2024

Abstract Kapok fibers (KFs) exhibit a distinctive hollow tubular structure and hydrophobic surface, positioning them as intriguing materials with a leading role in developing new materials for various applications. In this study, KFs from *Ceiba speciosa* trees underwent modification with soy lecithin (SL) and graphite (G) particles. The wax on KFs primarily comprised hydrophobic compounds, including bis(2-ethylhexyl) phthalate, *N*–*N*-dimethyldodecanamide and 1-chloro-dodecane. These compounds interacted favorably with the alkyl chains of SL, exposing the SL charge groups to the medium, as confirmed by X-ray photoelectron spectroscopy (XPS) and wettability increase. Incorporating SL and G particles to the KFs improved their thermal stability and charring capability. KFs modified with SL and G (at 13 wt% or 16 wt%) were added to aqueous solutions of hydroxypropyl methylcellulose (HPMC) at 30 g L^{-1}, forming homogeneous dispersions that were molded and oven-dried to create xerogel composites. Regardless of the G content, all xerogels exhibited compressive elastic modulus of 23 ± 1 kPa, maximum strain of 60% strain at $5.6 \pm$ kPa stress, and after unloading, the xerogels recovered 77% of their original height. Their porosity amounted to 68 ± 3%. The xerogels showed a maximum sound absorption coefficient (SAC) of approximately 0.6 at 2 kHz, making them interesting sustainable materials for building and architecture. Surface resistivity and volume resistivity values amounted to 3.8×10^8 Ω/square and 8.84×10^8 Ω cm, respectively, indicating that the xerogel composites displayed antistatic properties and potential application as packing material.

Keywords XPS · Sound absorption · Antistatic property · Compressive strain

Supplementary Information The online version contains supplementary material available at https://doi.org/10.1007/s10570-024-06113-2.

D. M. F. Sandrini · D. F. S. Petri (✉)
Department of Fundamental Chemistry, Institute of Chemistry, University of São Paulo, Av. Prof. Lineu Prestes 748, Sao Paulo 05508-000, Brazil
e-mail: dfsp@iq.usp.br

D. M. F. Sandrini
e-mail: daiana_dmf@hotmail.com

M. F. Pillis · O. V. Correa
Nuclear and Energy Research Institute, IPEN/CNEN-SP, Av. Prof. Lineu Prestes 2242, São Paulo 05508-000, Brazil
e-mail: mfpillis@ipen.br

O. V. Correa
e-mail: ovcorrea@ipen.br

P. Madesh · B. Krishnasamy
Polymer Engineering Laboratory, Department of Chemistry, PSG Institute of Technology and Applied Research, Coimbatore 641062, India
e-mail: priyanka@psgitech.ac.in

B. Krishnasamy
e-mail: balaji.psgtech@yahoo.co.in

Introduction

Kapok fiber (KF) is a natural plant fiber obtained from the seed hairs of the *Ceiba speciosa* or *Ceiba pentandra* trees. The Ceiba species are native to tropical rainforests in Central and South America, as well as parts of Africa and Asia (Zheng et al. 2014). The use of KF from *Ceiba speciosa* aligns with the growing interest in sustainable and renewable materials as an alternative to synthetic options. The tree's cultivation does not typically require intensive agricultural practices (Tropical Plants Database). The hollow tubular structure of KFs give them lightweight and buoyant characteristics, making them suitable for filling life jackets, pillows, mattresses, and cushions (Zhang et al. 2013). The wax layer on its surface makes KF suitable as an absorbent for oil and organic pollutants (Zheng et al. 2014; Lugito et al. 2020). KFs are also known for their thermal insulation and acoustic properties (Zheng and Wang 2014; Zheng et al. 2014).

Various strategies have been employed to modify the chemical modification of KF surface to expand its application field (Futalan et al. 2022; Zhang and Tang 2023). Most of them involve the previous removal of the oleophilic layer that covers the fiber surface to improve its wettability and adhesion properties. The pre-treatment of KFs with HCl and NaOH proved to a successful strategy to remove wax, lignin, hemicellulose, and impurities, exposing the hydroxyl groups (Abdullah et al. 2019; Wang et al. 2014; Sartika et al. 2020). Oxidation pre-treatments using chlorine-based oxidant agents also promoted the elimination of wax, lignin, and hemicellulose, turning KFs hydrophilic (Wang et al. 2016) and rough (Wolok et al. 2019). After the pre-treatment, the surface of KFs can be further modified to promote the creation of a new layer for a desired application (Futalan et al. 2022). However, there is scarce information on the modification of KF without a pre-treatment. For instance, the modification of KF with cetyltrimethylammonium bromide, a cationic surfactant, promoted the orientation of the positively charged head to the aqueous medium facilitated the polymerization of acrylonitrile on the KF surface (Fan et al. 2012). However, the modification of KF through the deposition of soy lecithin (SL) has not been reported so far. SL is a natural emulsifier and stabilizer derived from soybeans. It is often used in the food industry to improve the texture, shelf life, and mixability of various products. The hypothesis is that the hydrophobic chains of SL adsorb on the oleophilic layer of KF, exposing the charged phosphatidyl and quaternary ammonium groups to the medium, thereby increasing the hydrophilicity of the KFs and improving its wettability in aqueous media.

Graphite (G) is a crystalline form of carbon consisting of layers of carbon atoms linked by sp^2 bonds arranged in a hexagonal lattice. The incorporation of G particulate to fibers has been shown to have several potential benefits, including (i) reducing wear rates and friction coefficients (Hashmi et al. 2007), (ii) enhancing mechanical properties (Oladele et al. 2020; Dhanunjayarao et al. 2021), and (iii) imparting antistatic properties (Chen et al. 2022; Mishra et al. 2022). Dicyandiamide coated KFs were calcined at 600 °C to obtain G-C_3N_4 with excellent photocatalytic properties (Hu et al. 2020). Kim and co-workers (2018) demonstrated that loading flake G into basalt fiber-reinforced epoxy composite increased the elastic modulus of the composites by up to 83% and the thermal conductivity to a maximum value of 0.949 W mK^{-1}. G/bamboo flour/high-density polyethylene composites presented antistatic properties; when the G content was 12 wt%, the surface resistivity (ρ_S) and volume resistivity (ρ_V) decreased to 9.44×10^4 Ω and 5.89×10^5 Ω m, respectively, due to the creation of G conductive paths (Zhou et al. 2015). In this work, KFs were modified through the simultaneous incorporation of SL and G particles onto the surface. To comprehend the interactions governing the assembly of KF, SL, and G particles, analysis of the chemical composition of KF from *Ceiba speciosa* and its extractives was conducted. Additionally, surface chemical composition, structural aspects, wettability, and thermal properties were investigated.

Due to its eco-friendly nature, KF holds significant potential for application in the development of environmentally friendly materials tailored for specific applications. For this reason, SL and SL/G modified KFs were further combined with aqueous solutions of hydroxypropyl methylcellulose (HPMC) polymer, yielding moldable materials that upon oven-drying became xerogel composites. The demonstrated sound absorption capacity and antistatic electricity of the resulting xerogels underscore their potential application as building and packing materials.

Materials and methods

Materials

Kapok fibers (KF) were collected from the fruits of *Ceiba speciosa* in São Paulo (geographical coordinates 23° 33′ 0″ S, 46° 38′ 0″ W, Brazil), during the period from April to July. The chemical composition of KF was determined in duplicate according to the Renewable Energy Laboratory (NREL), following the TP-510-42618 protocol (Sluiter et al 2011) and standard TAPPI T222 om-02 method (Acid-Insoluble Lignin in Wood and Pulp), as 51.6 ± 2.3% cellulose, 17.2 ± 1.2% hemicellulose, 19.4 ± 1.6% lignin, 7.1 ± 1.4% extractives, 0.5 ± 0.1% ashes, and 4.2 ± 0.5% humidity. This composition is similar to the composition of KF reported in the literature (Draman et al. 2014).

Wax extraction (extractives) from the surface of KFs was carried out in duplicate using the Soxhlet apparatus, following TAPPI T204 cm-97 standard (Solvent Extractives of Wood and Pulp) with some modifications. Approximately 2.5 g of the cryogenically ground sample was loaded into filter paper and inserted into the extractor. Subsequently, the system was loaded with 200 mL of 70% v/v ethanol, and the extraction proceeded over a period of 12 h, maintaining 3 to 4 cycles per hour of extraction. Following the extraction period, the solvent containing the extractives was evaporated to a volume of 20 mL and transferred to a clean, pre-weighed flask. The sample was dried at room temperature until nearly dry, and then placed in an oven at 105 ± 3 °C to ensure complete solvent evaporation. Subsequently, the sample was cooled in a desiccator to achieve a constant mass and weighed for the determination of the extractives content.

For the determination of the chemical composition of the extractives, the sample was dried at room temperature until complete solvent evaporation and then redispersed in chromatographic dichloromethane for analysis by gas chromatography-mass spectrometry (GC–MS). The analyses were conducted using a Shimadzu QP2020 instrument (Shimadzu, Kyoto, Japan) equipped with an electron impact ionization (EI) operating at 280 °C and a DB-5MS column of 30 × 0.25 mm (Agilent Technologies, Santa Clara, CA, USA) operating in a temperature range of 50–280 °C with a flow rate of 1.82 mL min^{-1}. The NIST software library was used for the qualitative identification of compounds present in the extractives.

Hydroxypropyl methylcellulose (HPMC E4M, DS 1.9, MS 0.25, and M_w 2.5×10^5 g/mol) (Marani et al. 2015) provided by Dow Chemical (Brazil), food grade liquid soy lecithin (SL, 12 wt% of lipids, Gringer Ltd, Brazil), and ethanol (EtOH, Labsynth, Brazil) were used as received. Natural graphite particles (G) were purchased from Quimidrol Com. Ind. LTDA and were sieved to obtain particle size less than 38 µm. SEM images showed that the natural G particles have irregular sizes and shapes (Supporting Information SI1a).

Modification of KFs and preparation of the KF/SL and KF/SL/G xerogels.

Figure 1 shows schematically the modification process of KFs with SL and G. First, SL (10.0 g) was dispersed in 50 mL of 70% v/v ethanol using an ALB 260 H homogenizer (Inbras) operating at 250 rpm for 20 min. Afterwards, 1.2 g of dry KFs were immersed in the SL dispersion and stirred for 10 min to obtain KFs well dispersed in the medium. The SL modified KFs were placed in a Petri dish and dried in an oven at 60 °C until constant mass; they were coded as KF/SL**.** The content of KF in dry KF/SL was 10.7 wt%. The KFs were also modified by graphite particles (G) in the presence of SL. For that, 1.2 g of dry KFs were immersed into 50 mL of 70% v/v ethanol containing SL (10.0 g) and G at two different contents, namely, 2.4 g (~ 18 wt%), and 3.2 g (~ 22 wt%). The dispersions were stirred for 10 min and dried at 60 °C until constant mass. The modified fibers were coded as KF/SL/G18 and KF/SL/G22.

For the preparation of the composite xerogels, the dry modified KFs (0.8 g) were incorporated into 10.8 mL of a previously prepared 30 g L^{-1} HPMC solution, stirred with a glass baguette for 20 min to obtain a homogeneous mixture, molded into cylindrical acrylic molds and dried at 60 °C overnight (Fig. 1). The content of modified KFs in the dry system was 71.2 wt%. The final contents of G particles in the xerogels prepared with KF/SL/G18 and KF/SL/G22 amounted to 12.6 wt% and 16.0 wt%, respectively; the samples were coded as X-KF/SL/G13 and X-KF/SL/G16, respectively.

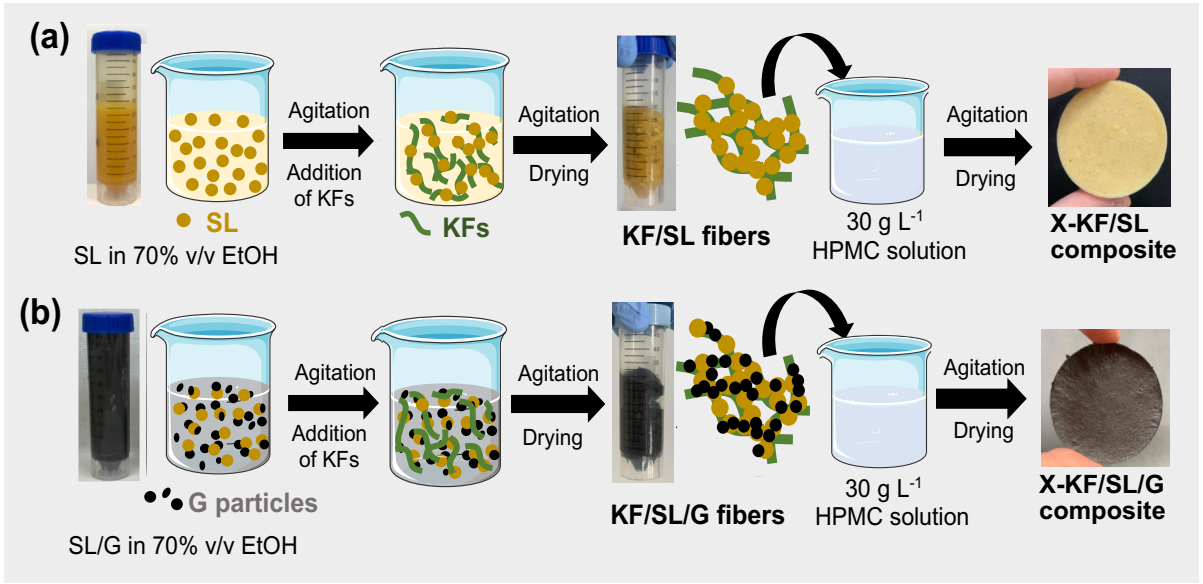

Fig. 1 Schematic representation of the modification of KFs with SL and G particles, and the preparation of **a** X-KF/SL and **b** X-KF/SL/G composite xerogels

Characterization of the modified KFs and the corresponding xerogels

SEM analysis was performed for G particles, KF, modified KFs and corresponding xerogels coated with gold (~5 nm) in a Jeol Neoscope JCM-5000 microscope operating at 10 kV or in a FESEM JEOL JSM-7401F equipment operating at 5 kV. At least ten fibers were analyzed to estimate a mean value of diameter. For xerogels, the cross-section samples were obtained by brittle fracture by cooling in liquid nitrogen. Brightfield and fluorescence microscopic observations of the modified KFs were performed using an inverted microscope Axiovert 200 M (Carl Zeiss, Germany) equipped with a LD Plan-Neofluar 40x/0.6 objective. Fibers were excited using the excitation DAPI filter set (365 nm) and the emission was observed in wavelength range of 420–490 nm.

Elemental analysis (Perkin Elmer 2400) was performed for KF and KF-SL for the determination of carbon, nitrogen and hydrogen content. Fourier transform infrared (FTIR) vibrational spectroscopy analysis was performed for KF, SL, modified KF and xerogel composites in the attenuated total reflection (ATR) mode, using a ZnSe crystal, and a Frontier Perkin Elmer FTIR-ATR equipment; the spectra were obtained with an accumulation of 32 scans and resolution of 4 cm^{-1}. The point of zero charge (pzc) of KF and KF/SL was determined by titration (Mahmood et al. 2011) (details provided as Supporting Information SI2).

Contact angle (θ) measurements were performed by the sessile drop method (SEO Phoenix – I, Korea) at 24 ± 1 °C, using droplets (7 µL) of MilliQ water placed on the horizontal plane of the fibers prepared on a flat glass surface. At least five samples were measured to determine the mean static contact angle. All measurements for KFs were performed 60 s after the droplet deposition. Longer exposition time did not change the drop shape. In the case of KF/SL and KF/SL/G fibers, after 3 s the water droplet was completed sorbed by the fibers.

TG/DTG curves were obtained for KF, SL, modified KFs, and xerogel composite in the temperature range from 30 to 800 °C, using platinum crucibles, under air atmosphere (60 mL min^{-1}) and heating rate of 10 °C min^{-1} using a TGA Q500 TA thermobalance.

The apparent density (ρ_{ap}) of the xerogels was determined by measuring the mass and volume of the samples at 23 ± 2 °C and relative humidity of 70 ± 10%. The mass was measured using an analytical balance and the volume was obtained by measuring the diameter and the length of the samples at different positions

using a pachymeter and micrometer. At least six samples of each specimen were used to obtain the average density value.

The pore size distribution, specific surface area (A_{sp}) and porosity were determined using mercury intrusion porosimetry (AutoPore IV 9500 analyzer Micromeritics Instruments Co., USA). The pore diameter (*D*) into which Hg was intruded was determined using the Washburn equation (Washburn, 1921):

$$P = -\frac{4\sigma cos\theta}{D} \quad (1)$$

where P is the external pressure (ranging from 3.58 kPa to 414 MPa), σ is the Hg surface tension (485 mN m^{-1} at 25 °C) and θ is the contact angle of Hg, which for most surfaces is 130°. Additionally, assuming that the pores have circular cross section, pore specific surface area (A_{sp}) was determined from the ratio between maximum volume of Hg intruded (V_i) and the pore diameter (D):

$$A_{sp} = \frac{4V_i}{D} \quad (2)$$

The swelling degree (SD) values were determined for the modified fibers and corresponding xerogels as a function of time with a precision tensiometer Krüss K100 at 24.0 ± 0.5 °C, dividing the mass of MilliQ water sorbed (pH 6.0) at equilibrium (m_{water}) by the mass of the dry adsorbent (m_d):

$$SD = \left[\left(\frac{m_{water}}{m_d}\right)\right] \quad (3)$$

The X-ray diffraction patterns of unmodified KF, KF/SL, KF/SL/G18, KF/SL/G22 fibers and G particles were recorded at 0.2°min^{-1}, in the 2θ range from 5° to 45° using a Rigaku-MiniFlex® diffractometer with a horizontal goniometer of high angle, operating at 30 kV/15 mA, and Cu K_α radiation (λ = 1.5418 Å). All data were subtracted from a blank run that consisted of measuring the empty sample holder under the same conditions used for the samples. The crystallinity index (CrI) was calculated from Eq. (4) (Segal et al. 1959):

$$CrI = 100 \times \left(\frac{I_{200} - I_{am}}{I_{200}}\right) \quad (4)$$

where I_{am} is the intensity of the minimum between (110) and (200) peaks of cellulose Iβ, at ~18.3°, and I_{200} is the maximum intensity of the (200) peak.

X-ray photoelectron spectroscopy (XPS, Specs, Germany) analysis was performed for KF, KF/SL and X-KF/SL, X-KF/SL/G13 and X-KF/SL/G16 xerogels. The X-ray source was monochromatic AlKα 1486.71 eV. XPS high resolution spectra of C 1s, N 1s, O 1s, and P 2s were obtained with a pass energy of 40 eV and 0.2 eV/step, accumulating 30, 40 or 50 scans. The spectra were deconvoluted using the CasaXPS® software. All binding energies in the XPS spectra were calibrated with respect to the C 1s peak (284.8 eV).

Dynamic mechanical analysis (DMA, TA Q800) was performed to investigate the mechanical properties of the xerogels at (25 ± 1) °C. At least six samples 7 mm thick and with diameter of 34 mm were analyzed. DMA analyses were conducted in compression mode using a uniaxial compression force ranging from 1 to 18 N at constant rate force of 1 N min^{-1} and preload force of 0.001 N.

The acoustic behavior of X-SL/KF and X-SL/KF/G xerogel samples (diameter 26 mm, mean height 7 mm) was investigated according to standards ISO 10534-2 1998 and ASTM E2611-09. Normal incidence absorption coefficient (SAC) of the materials was measured at room temperature in the one-third octave bands by using a steel impedance tube equipped with two microphones Bruel & Kjaer (type 4971-H 041) and a Data Acquisition System (Bruel & Kjaer LAN-XI type 3677-A-041). The sound absorption properties were determined in the frequency range of 100 Hz to 6.3 kHz. Measurements were carried out in triplicate with the sound wave propagating directly on the most porous side of the samples. The SAC values represent the average of six measurements for each sample. The noise reduction coefficient (NRC) was calculated as the average of the SAC values measured at 250, 500, 1000, and 2000 Hz.

The surface resistivity (ρ_S) and volume resistivity (ρ_V) tests were performed for the xerogels at 100 V using circular samples measuring 10 cm in diameter and 0.6 cm in thickness, at room temperature. These measurements were carried out according to the ASTM D257, using a Fischer Elektronik TE50.

Statistical analysis

Experimental results were expressed as the mean value and the corresponding standard deviation (mean ± SD). All data were analyzed by ANOVA (one-way analysis of variance) to assess differences among the groups and p values < 0.05 were classified as statistically significant. At least three independent experiments were carried out for each assay.

Results and discussion

Characterization of the modified KF

Figure 2a and b shows typical SEM images of pristine KFs from *Ceiba speciosa.* The fibers presented smooth surface, with a hollow lumen measuring (24 ± 6) μm in width and fiber wall thickness of (1.0 ± 0.1) μm. These dimensions are similar to those determined for KFs from *Ceiba pentandra* (Tao et al. 2021; Futalan et al. 2022). After the immersion in the SL dispersion, the resulting KF/SL fibers became rough (Fig. 2c, d), the terminal of some fibers were closed (yellow arrow in Fig. 2e) and some fibers appeared connected by joint points, as indicated in the yellow circles in Fig. 2e. The KF/SL/G18 and KF/SL/G22 fibers presented joint points, indicated by the yellow circles (Fig. 2f), and particles agglomerated on the surface (Fig. 2g, h), which were attributed to the G particles (Supporting Information SI1a). The joint points between fibers were probably originated from van der Waals and dipole–dipole interactions among the SL molecules and G particles deposited on the fibers. Such changes of morphological features indicated that SL and G particles were adsorbed on the surface of KF fibers.

The CG-MS chromatogram for the extractives from the surface KFs indicated the dominant presence of gamma-sitosterol, bis(2-ethylhexyl) phthalate, stigmast-4-en-3-one, squalene, cholest-4-ene-3,6-dione, 1-chloro-dodecane, and N–N-dimethyldodecanamide (Supporting Information SI3). When these hydrophobic compounds are on the surface of KF, they facilitate hydrophobic interactions with the SL alkyl chains.

The fluorescence (FM) and optical microscopy (OM) images in Fig. 3a and b, respectively, showed the hollow lumen of KF and the presence of lignin due to the bright emission of bluish tones when excited at a wavelength of 365 nm (Maceda and Terrazas 2022). After the interaction between KF and

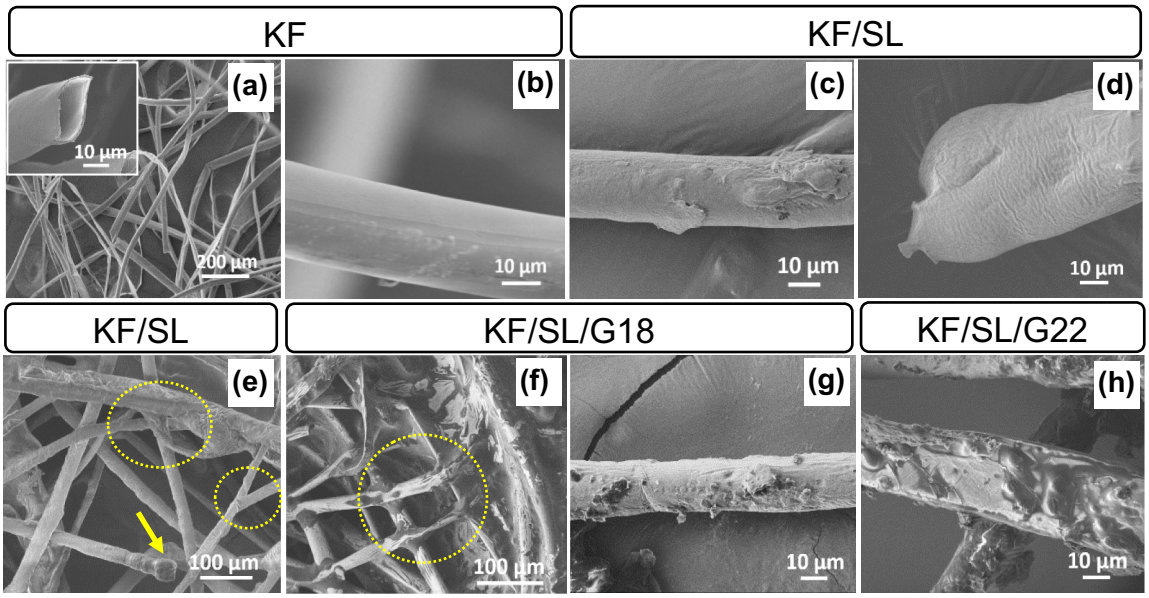

Fig. 2 SEM images of raw KFs (**a**, **b**), KF/SL (**c, d, e**), KF/SL/G18 (**f, g**), and KF-SL/G22 (**h**). The inset in (**a**) is a high magnification of the hollow lumen of KF. The yellow arrow in (**e**) indicates the closed lumen. The yellow circles in (**e**) and (**f**) indicate joint points between fibers

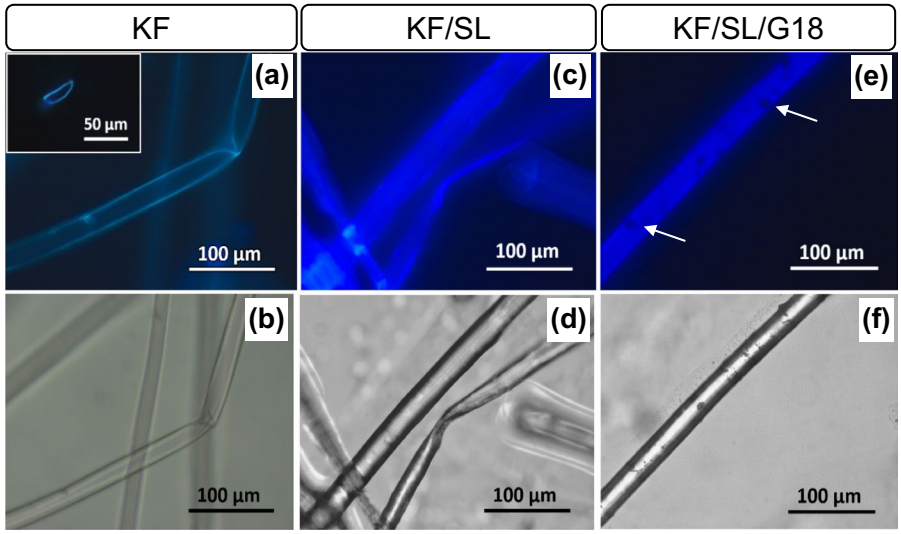

Fig. 3 Fluorescence (FM) and optical microscopy (OM) images of **a**, **b** KF; the inset in (**a**) shows the fluorescence emitted at excitation wavelengths of 365 nm by the lignin molecules present in the KF; **c**, **d** KF/SL and **e**, **f** KF/SL/G18; the white arrow in (**e**) indicates the presence of black dots, which were attributed to the G particles

SL, the lumen remained hollow (Fig. 3c, d), indicating that SL molecules were deposited only on the surface, they did not penetrate inside the fiber. Similarly, KFs treated with SL and G showed black dots distributed randomly on the surface (Fig. 3e, f), which were attributed to the G particles.

The swelling degree (SD) values for KF/SL, KF/SL/G18 and KF/SL/G22 fibers in MilliQ® water (pH 6) as a function of time (Supporting Information SI4) indicated that after 780 s the SD values amounted to 4.06 ± 0.54 g_w/g, 3.21 ± 0.26 g_w/g, and 3.46 ± 0.28 g_w/g, respectively (Table 1). A statistically significant difference between the mean SD values ($p = 0.013$) indicated that the inclusion of G particles reduced the affinity of KF/SL for water. One plausible explanation for this observation is that favorable interactions between SL molecules and G particles result in fewer charged groups being oriented towards the medium, thereby decreasing the overall affinity for water.

The swelling kinetics experiments were not possible for the pristine KFs because they are coated by hydrophobic components (Hori et al. 2000; Praba Karana et al. 2011), as evidenced in the Supporting Information SI3. The contact angle determined for MilliQ® water droplets on pristine KFs amounted to $121° \pm 2°$ (Supporting Information SI5), confirming the high hydrophobicity of KF (Zhang et al. 2013; Purnawati et al. 2018). On the other hand, KF/SL, KF/SL/G18 and KF/SL/G22 fibers were completely wetted by water after 3 s (Supporting Information SI5). The hydrophilicity of KF/SL and KF/SL/G is probably due to the SL charges. KF/SL presented two points of zero charge (pzc) (Supporting Information SI2), namely, at pH ~ 2, assigned to the 1st ionization equilibrium of the phosphoric acid, and at pH ~ 6.7, associated to the ionization of the amine group

Table 1 Swelling degree (SD) values for KF/SL, KF/SL/G18 and KF/SL/G22 and CHN elemental analysis values for KF, SL and KF/SL

Sample	SD (g_w/g)*	%C	%H	%N	N/C
KF	–	44.76 ± 0.04	5.8 ± 0.2	0.31 ± 0.05	0.0069
SL	–	66.0 ± 0.1	10.3 ± 0.1	0.78 ± 0.02	0.0118
KF/SL	4.06 ± 0.54	63.2 ± 0.2	9.0 ± 0.2	0.87 ± 0.05	0.0138
KF/SL/G18	3.21 ± 0.26	–	–	–	–
KF/SL/G22	3.46 ± 0.28	–	–	–	–

*Equilibrium SD values for MilliQ® water (pH 6) after 780 s, at 23 ± 2 °C

belonging to the phosphatidylethanolamine. The pzc of 6.7 is similar to values reported for SL in the literature (Fischgold and Chain 1934; Robinson 1960). Thus, at pH 6 (MilliQ® water), the KF/SL surface is expected to be positively charged.

Table 1 shows the CHN elemental analysis determined for KF, SL, and KF/SL. The N content of (0.31 ± 0.05)% allowed calculating the amount of (1.9 ± 0.3)% of protein (Hames et al. 2008) in the KFs; it is similar to the value of 2.1% reported in the literature for KF from other *Ceiba* tree species (Smole et al. 2013). SL contains predominantly inositol phosphatides, phosphatidylcholine and phosphatidylethanolamine in its composition, the last two contain quaternary ammonium and amine groups, respectively (Scholfield 1981). KF/SL presented the highest N/C ratio, indicating that SL was successfully attached on the KF surface.

The FTIR-ATR spectra obtained for KF/SL showed the characteristic bands of KF and SL. KF presented cellulose characteristic bands, a broad band in the 3600–3300 cm^{-1} region (OH vibrational stretching), bands at 2918 and 2852 cm^{-1} (asymmetrical and symmetrical C–H stretching of methylene), 1733 and 1372 cm^{-1} (C=O stretching) that might be attributed to carboxylic groups and esters in lignin, and acetyl groups in hemicellulose and extractives, 1595 and 1505 cm^{-1} that are characteristic of vibrations of lignin aromatic ring, 1425 cm^{-1} (C–H bending of hemicellulose and lignin), 1238 cm^{-1} due the stretching vibration of phenolic group in lignin and in the 1100–900 cm^{-1} region assigned to the C–O and C–H stretching vibrations of the glucopyranose ring (Silverstein et al. 2014). The complete band assignment was provided as Supporting Information SI6. Particularly, the spectrum of KF/SL presented bands at 2922 cm^{-1} and 2850 cm^{-1} with relatively high intensity, which were assigned respectively to the C–H asymmetric and symmetric stretching vibrational modes of methyl and methylene groups belonging to the alkyl chains of the SL lipids (Michał et al. 2015; Shah et al. 2018).

Figure 4a shows the XRD pattern of unmodified KF. It presented superimposed peaks (1–10)/(110) in the 2θ region of 15° to 16.5°, an intense peak at 22.2° related to the (200) plane due to the crystalline domains of cellulose and a small diffraction peak near 35°of (004) plane; these features are typical for cellulose Iβ (French 2014). The CrI value was estimated as 53% (Supporting Information SI7), which is slightly higher than the 47.6% reported by Zhang and Tang (2023). The XRD pattern of KF/SL (Fig. 4a) showed diffraction peaks at 11.5° and 20.8°, which correspond to the SL pattern (Zhang et al. 2015), indicating the successful coating of SL on KFs. A similar trend was observed for SL coated bacterial cellulose nanofibers (Zhang et al. 2015).

The XRD patterns of KF/SL/G18 and KF/SL/G22 in Fig. 4b revealed a broad diffraction peak at 20.6° related to SL, and a sharp and intense diffraction peak at 26.7° characteristic of the graphite (002) diffraction plane (Li et al. 2007; Azevedo et al. 2015; Zhang et al. 2020) (Supporting Information SI1b). The intensity of the diffraction peak at

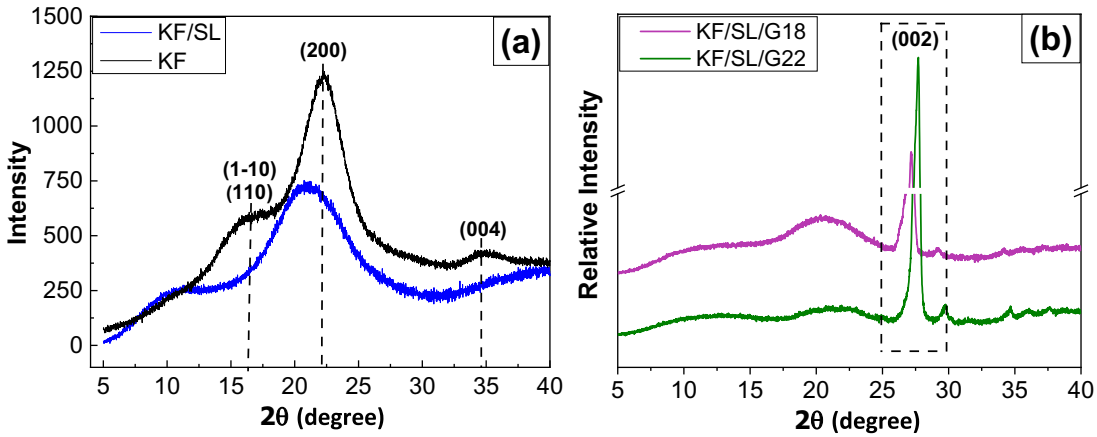

Fig. 4 XRD patterns of **a** KF and KF/SL, and **b** KF/SL/G18 and KF/SL/G22 fibers

26.7° increased with the increase of graphite content from 18 to 22 wt%.

Figure 5a and b show the TG and DTG curves, respectively, determined for KF, SL, KF/SL, KF/SL/G18, and KF/SL/G22, under air flow and heating rate of 10 °C min^{-1}. Table 2 summarizes the thermal events with the corresponding mass loss, and the residual mass at 800 °C.

TG/DTG curves of pristine KFs revealed a first mass loss (4.4%) in the range of 25–110 °C due to water release. The thermal degradation of the fiber started at 260 °C, presenting a slight shoulder around 300 °C with 29.3% mass loss, that is characteristic of the thermal degradation for hemicelluloses (Yao et al. 2008; Spinacé et al. 2009) (Table 2). The main degradation peak (T_{peak2}) at 354 °C with 80.8% mass loss was associated with the major thermal decomposition of cellulose (Yao et al. 2008; Monteiro et al. 2012), the majority constituent of the fiber. The degradation third event with 95.3% mass loss occurred in the range from 380 to 590 °C (T_{peak3} equal 576 °C) and was attributed to the final degradation of lignin (Rashid et al. 2016) followed by formation of a charred residue. The residual mass was 5.6% at 800 °C. For comparison, Tao and co-workers (2021) reported similar thermal events and residual mass of 7.9% at 800 °C in air atmosphere for a commercial KF.

SL showed three thermal events at 219 °C, 321 °C, and 385 °C (with ~85% total mass loss), that are related to the degradation of SL components (Table 2). Similar thermal degradation behavior was

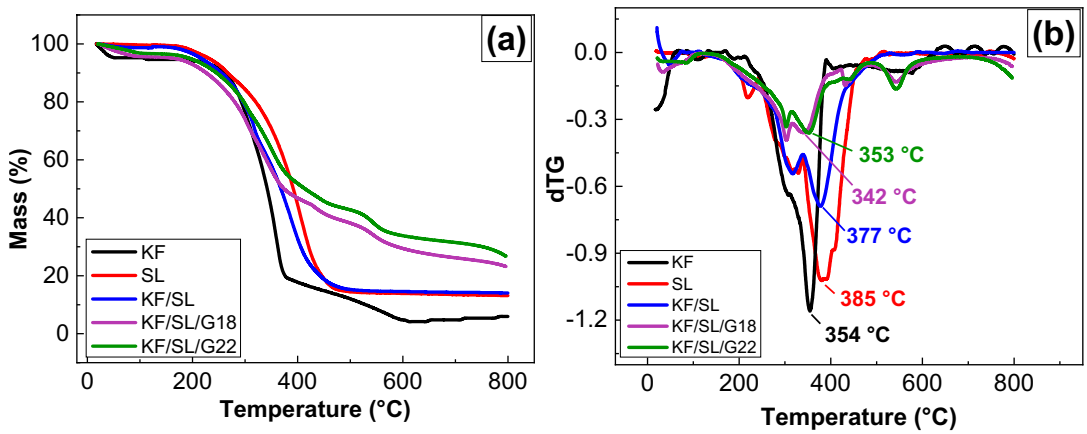

Fig. 5 **a** TG and **b** corresponding DTG curves determined for KF, SL, KF/SL, KF/S/G18 and KF/SL/G22 under air flow (60 mL min^{-1}) and heating rate of 10 °C $min.^{-1}$

Table 2 Thermal degradation events determined for KF, SL, KF/SL, KF/SL/G18, and KF/SL/G22 using thermogravimetric analysis under air atmosphere (60 mL min^{-1}), and heating rate of 10 °C min^{-1}

Sample	1st event		2nd event		3rd event		4th event		Ash % (800 °C)
	T_{peak1} (°C)	wt.% loss	T_{peak2} (°C)	wt.% loss	T_{peak3} (°C)	wt.% loss	T_{peak4} (°C)	wt.% loss	
KF	306	29.3	354	80.8	576	95.3	***	***	5.90
SL	219	6.8	321	31.4	385	87.3	***	***	11.3
KF/SL	317	38.9	377	85.7	***	***	***	***	14.0
KF/SL/G18	303	32.3	342	54.6	432	60.8	542	76.6	23.4
KF/SL/G22	303	25.2	352	51.3	441	56.7	542	73.3	26.7
Graphite	819	55.4	***	***	***	***	***	***	63.1

T_{peak} stands for the peak thermal degradation temperature. The ash content refers to the residual mass at 800 °C. TG/DTG curves for graphite (G) particles were provided as Supporting Information SI8

reported by Merino and co-workers (2016) in studies with commercial SL. The residual mass at 800 °C was 11.3%; this relatively high residual mass is due to the presence of phosphate and quaternary ammonium groups in the chemical structure of SL. KF/SL fibers showed two peaks at 317 °C and 377 °C attributed to the main degradation of KF and SL. The higher degradation temperatures of KF/SL (T_{peak1} and T_{peak2}) compared to KF, as well as the increase in ash content from 5.9% (KF) to 11.3% (KF/SL) suggest that the van der Waals interactions between the hydrophobic compounds on the surface of KF and the SL alkyl chains probably drive the improved thermal stability of KF.

The KF/SL/G18 and KF/SL/G22 fibers presented first thermal events at ~300 °C and ~350 °C related to the main degradation of KF and SL, and additional degradation peaks in the range between 430–550 °C, with maximal mass loss of 72% due to the presence of graphite. The incorporation of G particles also increased the residual mass from 5.9 wt% (KF) to 23.4% (KF/SL/G18) and 26.7% (KF/SL/G22) due to the high thermal stability of G particles (T_{peak} = 819 °C; 63.1% of residual mass) (Supporting Information SI8). The presence of SL and G particles clearly improved the charring capability of KF. Zhang and Tao (2023) reported similar effect for the modification of KFs with 2 g or 4 g of ammonium dihydrogen phosphate (ADP); at 700 °C (in air flow) the char content increased from 1.5% (KF) to 26.6% and 31.9%, respectively, due the presence of ADP. However, the T_{peak} values of SL/G-modified KFs did not improve the thermal stability in comparison to KF/SL. One possible explanation is the favorable interaction between SL molecules and G particles, remaining less SL molecules to interact with KF layer surface.

Characterization and application of xerogel composites

In order to mold into desirable shape and size the KF/SL, KF/SL/G18, and KF/SL/G22 fibers were added to aqueous HPMC solution at 30 g L^{-1} and manually mixed until obtain a homogeneous mixture (Fig. 1). After drying at 60 °C until constant weight, X-KF/SL, X-KF/SL/G13, and X-KF/SL/G16 xerogels were characterized.

The swelling degree (SD) determined for X-KF/SL, X-KF/SL/G13, and X-KF/SL/G16 under equilibrium conditions amounted to 7.0 ± 0.8 g_w/g, 7.7 ± 0.9 g_w/g, and 5.1 ± 0.5 g_w/g, respectively (Supporting Information SI9). Compared to the SD values determined for the modified fibers (Table 1), the water sorption capacity of the xerogels increased due to the presence of HPMC, a hydrophilic cellulose ether. Noteworthy, it was not possible to measure the contact angle for water droplets on the xerogels because after the deposited on the surface, the droplets were immediately sorbed by the xerogels.

Figure 6 shows the SEM images of X-KF/SL, X-KF/SL/G13, and X-KF/SL/G16 xerogels taken from the surface and internal structure. The surface of all xerogels presented small pores and many KFs randomly distributed (Fig. 6a–c). Particularly on the surface of X-KF/SL/G13 it was possible to observe small particles, indicating the presence of G particles (Fig. 6b). Magnification of the surface of X-KF/SL/G16 (Fig. 6c, inset) showed that the hollow tubular structure of some KFs remained preserved even after the incorporation of HPMC to form xerogels. The SEM images taken from the internal structure of the xerogels evidenced large pores formed by entangled KFs and HPMC (Fig. 6d–f). The internal porous structure of the xerogels was also observed through digital photography of their cross-sections (Fig. 6g–i). The higher G content (X-KF/SL/G16) seems to have improved the compatibilization between KF, SL and G particles, leading to the emergence of continuous walls (Fig. 6f, i), which may have contributed to the reduction in SD values.

Supporting Information SI10 shows the FTIR-ATR spectra of KF/SL, X-KF/SL, X-KF/SL/G13, and X-KF/SL/G16. The characteristic bands of HPMC, KF, and SL were superimposed and no shift in the characteristic bands could be observed.

The TG/DTG curves obtained for pure HPMC, X-KF/SL, X-KF/SL/G13, and X-KF/SL/G16 xerogels under air flow are provided as Supporting Information SI11. Table 3 presents the thermal degradation events with the corresponding mass loss. All xerogels presented the 1st degradation peak in the range of 217–232 °C (shoulder) corresponding to 14.2% mass loss, which was attributed to thermal degradation of HPMC (Table 3) and a 2nd event in the range of 301–309 °C represented by an intense peak which corresponds to 58% mass loss due to the first

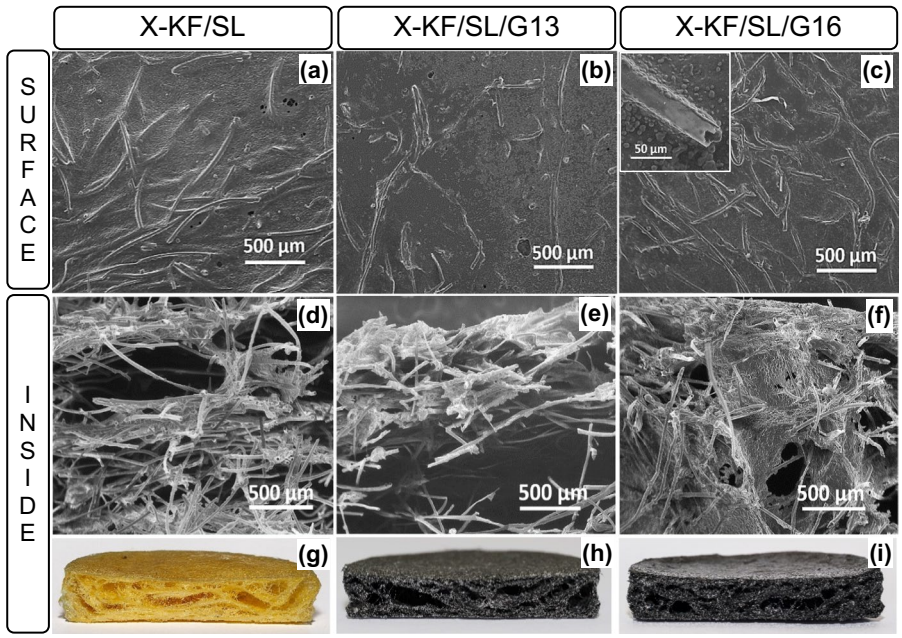

Fig. 6 SEM images of X-KF/SL, X-KF/SL/G13, and X-KF/SL/G16 xerogel composites taken form the surface **(a–c)** and internal structure (**d–f**). The inset in (**c**) is a zoom to show the hollow lumen of KF. Digital photographs of the cross-section of **g** X-KF/SL, **h** X-KF/SL/G13, and **i** X-KF/SL/G16 xerogel composites

Table 3 Degradation temperature peaks and mass loss corresponding to the thermal events, and the residual mass (ash content) at 800 °C determined from the TG and DTG curves obtained for X-KF/SL, X-KF/SL/G13, X-KF/SL/G16, and HPMC (powder) under air flow (60 mL min^{-1}) and heating rate of 10 °C min^{-1}

Sample	1st event		2nd event		3rd event		4th event		Ash % (800 °C)
	T_{peak1} (°C)	wt.% loss	T_{peak2} (°C)	wt.% loss	T_{peak3} (°C)	wt.% loss	T_{peak4} (°C)	wt.% loss	
HPMC	254	10.0	336	86.2	483	98.0	-	-	0.44
X-KF/SL	228	12.7	309	48.3	353–436	86.5	-	-	12.3
X-KF/SL/G13	230	12.7	301	59.5	444	68.3	571	77.5	14.6
X-KF/SL/G16	217	8.3	303	57.5	451	65.1	560	77.7	16.5

TG/DTG curves were provided as Supporting Information SI12

degradation stage of the KF (Table 2). In the 3rd thermal event, X-KF/SL xerogel showed shoulder peaks in the range of 353–436 °C with mass loss up to 86.5%, assigned to degradation of HPMC and SL (Table 2). The thermal behavior of X-KF/SL was similar to that of the corresponding modified fiber (KF/SL) (TG curves in Fig. 5a and Supporting Information SI11b) showing that the incorporation of HPMC in the xerogels did not affect the thermal stability of the KF/SL fibers. However, the ash content at 800 °C decreased from 14.1% (KF/SL) (Table 2) to 12.3% (X-KF/SL) due to the low ash content inherent to HPMC (0.44%).

Both X-KF/SL/G13, and X-KF/SL/G16 xerogels presented similar thermal behavior with ~68% to 78% mass losses in the range of ~440 °C to ~580 °C. In this temperature range, X-KF/SL presented 82% of mass loss at 436 °C. Therefore, the significant increase in the thermal stability might be attributed to an efficient incorporation of the G particles in the X-KF/SL systems. Furthermore, the ash contents of X-KF/SL/G13 and X-KF/SL/G16 at 800 °C amounted to 14.6% and 16.5%, respectively, which were superior to that of X-KF/SL (12.3%). The ash contents determined for the xerogels were lower than those observed for the KF/SL/G18 (23.4%) and KF/SL/G22 (26.7%) fibers (Table 2) due to the presence of HPMC.

The chemical composition on the surface of KF, KF/SL and X-KF/SL, X-KF/SL/G13 and X-KF/SL/

G16 xerogels samples was investigated by XPS. The chemical composition provided by the survey spectra (Table 4) indicated a small amount of nitrogen on the pristine KF due to the presence of extractives (N–N-dimethyldodecanamide) (Supporting Information SI3); N was also identified by CHN elemental analysis (Table 1). Compared to the pristine KF, KF/SL presented increase in oxygen content and decrease in the C/O ratio from 4.22 to 3.49, and the appearance of P, indicating the presence of SL phosphatidyl groups orientated to the air. In the case of X-KF/SL, X-KS/SL/G13 and X-KS/SL/G16 xerogels, the C/O ratios amounted to 2.95, 3.03, and 3.09, respectively, which are smaller than those determined for KF and KF/SL. This effect was attributed to the presence of HPMC (rich in hydroxyl groups) on the surface of the xerogels. N was detected only on the surface of X-KS/SL/G13 and X-KS/SL/G16 xerogels, indicating the orientation of SL quaternary ammonium and/or amine groups to the air. Small amounts of B and Si elements in the KF-SL and xerogels were attributed to the presence of these micronutrients in the soybean plant, raw material used for the production of SL (Alharby et al. 2021; de Paula et al. 2021).

Figure 7 shows the high-resolution XPS spectra for carbon (C 1s), oxygen (O 1s), nitrogen (N 1s) and phosphorus (P 2s) along with the Gaussian function fitting (CasaXPS® software). The area and binding energy peak position (eV) values were provided as Supporting Information SI12.

The deconvolution analysis of the C 1s spectrum for pristine KF revealed four distinct peaks attributed to C=C (283.8 eV), C–C (284.7 eV), C–O/C(C=O)/C–N (286.0 eV), and C=O (288.3 eV) bonds, corroborating with the compounds identified in the extractives (see Supporting Information SI3). The intensity of C 1s peaks in the KF/SL spectrum was higher than in the KF spectrum, providing clear evidence of SL incorporation onto KFs. The C 1s spectrum of X-KF/SL distinctly revealed the presence of HMPC chains in the outermost layer of the xerogels. This is evidenced by a notable increase in the intensities linked to the C–O/C(C=O)/C–N (285.9 eV) and C=O (288.6 eV) bonds. This observation could potentially elucidate the substantial rise in swelling degree values exhibited by xerogels when compared to modified fibers (Tables 1 and 3). Compared to X-KF/SL, the C 1s spectra of X-KF/G13 and X-KF/SL/G16 exhibited higher intensity in the C–C peaks, indicating the presence of G particles on the surface.

Concerning the O 1 s spectra, the intensity of the C=O/P=O (531.1 eV), C–O/C–O–P (532.1 eV), and C–O–C=O (533.2 eV) peaks observed in the KF spectrum significantly increased after the incorporation of SL onto the fibers. Notably, the P=O at 531.1 eV and C–O–P at 332.0 eV peaks were observed in the same binding energy (BE) region as C=O and C–O, respectively. The P=O bond, associated with the phosphate group of phosphatidylcholine and phosphatidylethanolamine, was only observed on the KF/SL spectrum.

In the N 1 s spectra, the pristine KF displayed three peaks at 397.8, 399.3, and 400.8 eV, corresponding to –C–N–C, C–N, and N–H bonds, respectively, which were attributed to the extractive compounds (Supporting Information SI3). The emergence of quaternary N 1s at 402.1 eV (X-KF/SL/G13) and 401.4 eV (X-KF/SL/G16) indicated the presence of phosphatidylcholine on the surface. Consequently, it can be inferred that SL molecules interacted not only with KF but also with G particles. Thus, the SL molecules act as compatibilizers between KF and G particles, and the presence of SL charged quaternary ammonium and phosphatidyl groups oriented to the air demonstrated effective interaction with the HPMC hydroxyl groups.

Figure 8 suggests possible interactions among the components present on the X-KF/SL/G xerogel

Table 4 Surface chemical composition determined by XPS for KF, KF-SL and X-KF/SL, X-KF-SL/G13 and X-KF/SL/G16 xerogels and the respective C/O and N/C ratios

Sample	Content (%)						Ratio	
	C	O	N	Si	B	P	C/O	N/C
KF	80.35	19.05	0.60	–	–	–	4.22	0.007
KF/SL	73.29	21.03	–	1.58	2.93	1.16	3.49	–
X-KF/SL	72.88	24.69	–	1.00	1.43	–	2.95	–
X-KF/SL/G13	72.86	24.02	0.37	1.89	0.85	–	3.03	0.005
X-KF/SL/G16	72.70	23.51	0.84	1.17	1.78	–	3.09	0.011

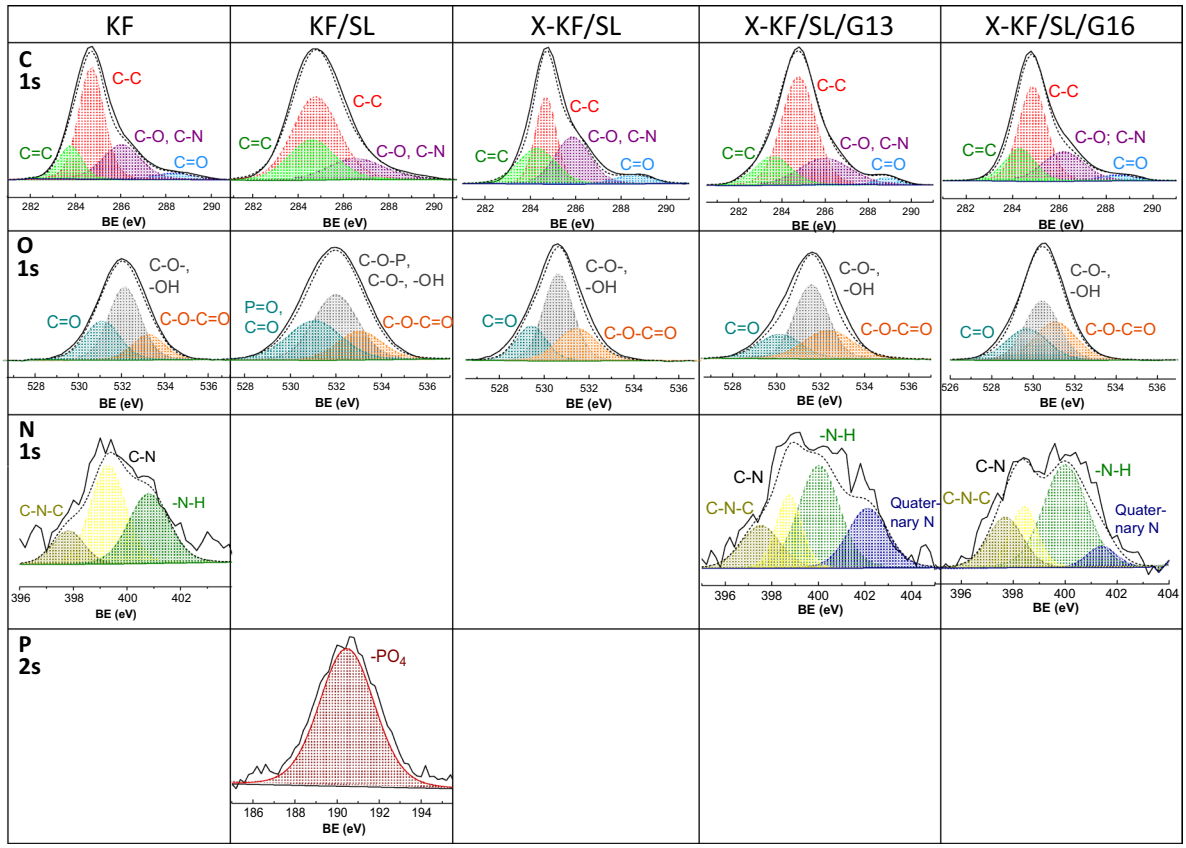

Fig. 7 High-resolution spectra C 1s, O 1s, N 1s, and P 2s for KF, KF/SL fibers, and X-KF/SL, X-KF/G13 and X-KF/SL/G16 xerogels

surface. The SL alkyl chains (R groups) interact with the hydrophobic components of KF wax and G particles by van der Waals forces. The orientation of the SL hydrophilic heads (charged groups) towards the air favors the interaction with the HPMC hydroxy groups (ion–dipole interactions).

The mechanical behavior of the xerogels was investigated under uniaxial compressive loading at constant force rate. All xerogels displayed the characteristic behavior of elastomeric foams under compressive loading (Cluff and Esmaeili 2009; Albuquerque et al. 2023), where three distinct deformation regimes were identified. The three regimes were: (i) a linear elastic behavior at low strain (up to 8% strain), (ii) a plastic yield plateau up to around 40% strain (Supporting Information SI13), where the stress increased slightly because of the non-reversible collapse of the structure of xerogels, and (iii) the densification, indicated by a stiffening and a reduction in the cushion factor of the materials (Cluff and Esmaeili 2009). The xerogels displayed a maximum of 60% strain at $5.6 \pm$ kPa stress (Supporting Information SI13). The compressive modulus (E) determined from the slope in the linear elastic region ranged from 22.3 ± 5.1 kPa to 24.7 ± 6.2 kPa (Table 5). The addition of G particles at concentrations of 13 wt% and 16 wt% had no significant effect on the stiffness of xerogels ($p = 0.829$). Similarly, there was no statistically significant difference among the values of apparent density (ρ_{ap}), porosity and surface area (A_{sp}) (Table 5) for the xerogels with and without G particles. The values of pore mean diameter for X-KF/SL, X-KF/SL/G13 were similar and larger than that for X-KF/SL/G16 xerogels. The increase in the G content to 16 wt% improved the compatibilization between KF, SL, and G particles,

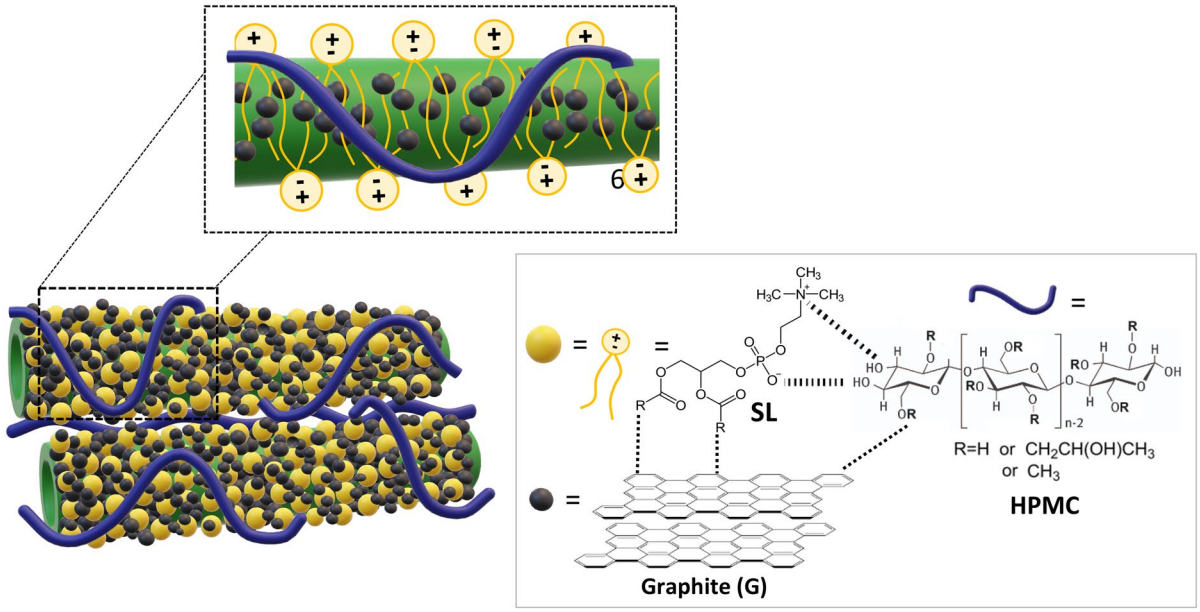

Fig. 8 Schematic representation of the possible interactions among the components present on the surface of the X-KF/SL/G xerogels. The SL alkyl chains (R groups) interact with the hydrophobic components of KF wax and G particles by van der Waals forces. The orientation of the SL hydrophilic heads (charged groups) towards the air favors the interaction with the HPMC hydroxy groups (ion–dipole interactions)

Table 5 Compressive modulus (E), apparent density (ρ_{ap}), porosity (%), surface area (A_{sp}), and pore mean diameter (D) determined for X-KF/SL, X-KF/SL/G13 and X-KF/SL/G16 xerogels

Sample	E (kPa)	ρ_{ap} (g cm^{-3})	Porosity (%)	A_{sp} (m^2 g^{-1})	D (μm)
X-KF/SL	24.7 ± 6.2	0.133 ± 0.002	71 ± 7	0.103 ± 0.010	80 ± 8
X-KF/SL/G13	23.8 ± 8.7	0.177 ± 0.005	65 ± 6	0.076 ± 0.008	73 ± 7
X-KF/SL/G16	22.3 ± 5.1	0.172 ± 0.009	68 ± 7	0.107 ± 0.011	43 ± 4

favoring the formation of continuous walls (Fig. 6f) and, consequently, smaller D values.

Figure 9 shows photographs of the xerogels taken during the compression tests. The structure was gradually collapsed with increasing load without lateral deformation of the samples. After 45 min that the load was removed, the xerogels recovered 77% of their original heights, indicating that only a small part of the material collapsed irreversibly.

To evaluate the acoustic properties of xerogels, the normal incident absorption coefficients (SAC) were determined in a Brüel & Kjaer apparatus taken at 1/3 octave intervals. Figure 10 shows that the SAC values gradually increased with the frequency between 0.1 kHz to 2 kHz. The low frequency (up to 0.8 kHz), the materials exhibit SAC values lower than 0.20, reaching a maximal value of 0.6 ± 0.1 at 2 kHz. As the sound frequency continues to increase, a gradual decrease was observed up to ~ 0.15 at 6.3 kHz. Therefore, the composite xerogels showed the best sound absorption capacity in the frequency range of 1.6 kHz to 4 kHz. The increase in sound-absorption properties as a function of frequency is characteristic of porous materials. As the frequency increases, friction and vibration between the pore structure and air gaps increases, leading to greater acoustic energy consumption and therefore greater sound absorption (Rao et al. 2011; Liu et al. 2015).

The addition of G particles to the xerogels at 13 wt% and 16.0 wt% had no statistically significant

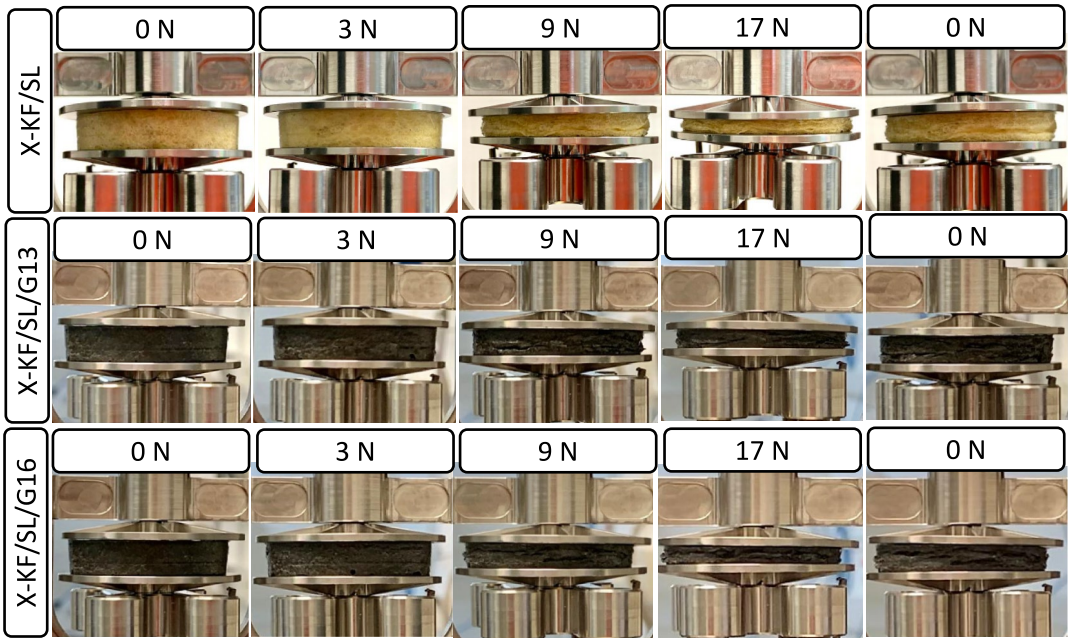

Fig. 9 Photographs of the xerogels before the compression tests (0 N), during the compression test when subjected to a load of 3 N, 9 N and 17 N, and after unloading (0 N).

effect ($p = 0.692$) on the mean SAC values. In the full frequency range (0.1–6.3 kHz), the mean SAC values amounted 0.26 ± 0.17 for X-KF/SL and 0.22 ± 0.13 and 0.25 ± 0.17 for X-KF/SL/G13 and X-KF/SL/G16, respectively. It might be because the xerogels presented similar porosity values (Table 6).

Table 6 Porosity (%), mean thickness (H), apparent density (ρ_{ap}) and sound absorption coefficient (SAC) measured at 250, 500, 1000 and 2000 Hz for X-KF/SL, X-KF/SL/G13, and X-KF/SL/G16 xerogels

Sample	Porosity (%)	H (cm)	ρ_{ap} (g cm^{-3})	SAC				NRC
				250 (Hz)	500 (Hz)	1000 (Hz)	2000 (Hz)	
X-KF/SL	71 ± 7	0.8	0.133 ± 0.002	0.13	0.15	0.20	0.52	0.25
X-KF/SL/G13	65 ± 6	0.6	0.177 ± 0.006	0.11	0.13	0.21	0.41	0.22
X-KF/SL/G16	68 ± 7	0.6	0.172 ± 0.009	0.25	0.14	0.22	0.50	0.28
KF assembly[(a)]	93–98	2.0	0.005	0.08	0.11	0.17	0.34	0.18
KF assembly[(a)]	93–98	2.0	0.015	0.09	0.16	0.41	0.79	0.36
KF assembly[(a)]	93–98	4.0	0.015	0.14	0.40	0.86	0.98	0.60
50%KF/50% PCL composite[(b)]	-	1.0	0.156	0.06	0.10	0.30	0.58	0.26
50%KF/50% PP MUC composite[(c)]	94	0.9	0.075	0.97	0.36	0.57	0.87	0.69
50%KF/50% PP MC composite[(c)]	90	0.6	0.910	0.91	0.34	0.60	0.89	0.68
90%KF/10% hollow polyester[(d)]	-	0.5	0.013	0.07	0.10	0.25	0.46	0.22
Hemp fiber assembly[(e)]	-	1.0	1.50	0.11	0.15	0.30	0.37	0.23
50% hemp/50% PCL[(f)]	-	1.0	0.30	0.02	0.05	0.30	0.53	0.23

For comparison, assemblies of KF[(a)] (Xiang et al. 2013), 50%KF/50% PCL composite[(b)] (Lyu et al 2020), 50% KF/50% PP composite[(c)] (Veerakumar and Selvakumar 2012), 90% KF/10% hollow polyester[(d)] (Liu et al. 2015), hemp fiber assemblies[(e)] (Zhang et al. 2022) and 50% hemp stalk/50% PCL[(f)] composite (Su et al. 2022). NRC corresponds to the arithmetic average of SAC values measured at 250, 500, 1000 and 2000 Hz

Table 6 shows the NRC values calculated as the average over the SAC values at 250, 500, 1000 and 2000 Hz for the xerogels prepared in this study and for other KF based materials, for comparison. The NRC values determined for X-KF/SL, X-KF/SL/G13, and X-KF/SL/G16 were comparable to those reported for 50%KF/50% polycaprolactone (PCL) (Lyu et al 2020) and 90% KF/10% hollow polyester (Liu et al. 2015) composites.

Veerakumar and Selvakumar (2012) reported that 50% KF/50% polypropylene (PP) fiber composites that were subjected to mechanical compression (MC) showed poorer acoustic performance at 250 Hz than the corresponding uncompressed materials (MUC). On the other hand, the slight reduction in porosity from 94 to 90% due to compression did not affect their NRC values. In comparison to pristine KF, Xiang and co-workers (2013) showed that the NRC values can be affected by both the bulk density and thickness of the fiber assemblies. For instance, they found that the NRC value of 0.36 determined for KF assemblies with a thickness of 2.0 cm and a density of 0.015 g cm^{-3}, was twice that of the assemblies with the same thickness but a lower density of 0.005 g cm^{-3} (resulting in an NRC of 0.18). Conversely, the NRC was 0.60 when the assemblies were 4.0 cm thick and had the density of 0.015 g cm^{-3}. The data presented in Table 6 suggest that thickness, density, and porosity are important parameters that modulate the microstructural characteristics of the absorber and affect the sound absorption property.

Compared to sound absorbers containing other lignocellulosic fibers, the xerogels developed in this study showed similar acoustic behavior to hemp fiber assemblies of higher density (1.5 g cm^{-3}) and thickness (1.0 cm) (Zhang et al. 2022). The use of hemp stalk (50 wt%) as reinforcement of PCL matrix resulted in 1.0 cm thick composites with density of 0.30 g cm^{-3} and an NRC value of 0.23 (Su et al. 2022), which is comparable to the KF based xerogels presented here (Fig. 10.

Table 7 presents the surface (ρ_S) and volume (ρ_V) resistivity values determined for X-KF/SL and X-KF/G13 xerogels. The ρ_S values ranged from 4.8×10^8 Ω/square to 9.1×10^8 Ω/square and ρ_V reached values of ~1.0×10^9 Ω cm, indicating that the xerogels have antistatic and dissipative properties according to DIN 54345. The XPS data revealed that the surface of the xerogel is enriched with SL quaternary ammonium groups (Fig. 7), facilitating charge transfer, and thereby inhibiting static charge accumulation on the material's surface (Lee 2013; Rezaei et al. 2022). In comparison to X-KF/SL, X-KF/SL/G13 exhibited lower values for ρ_S and ρ_V. The presence of graphite,

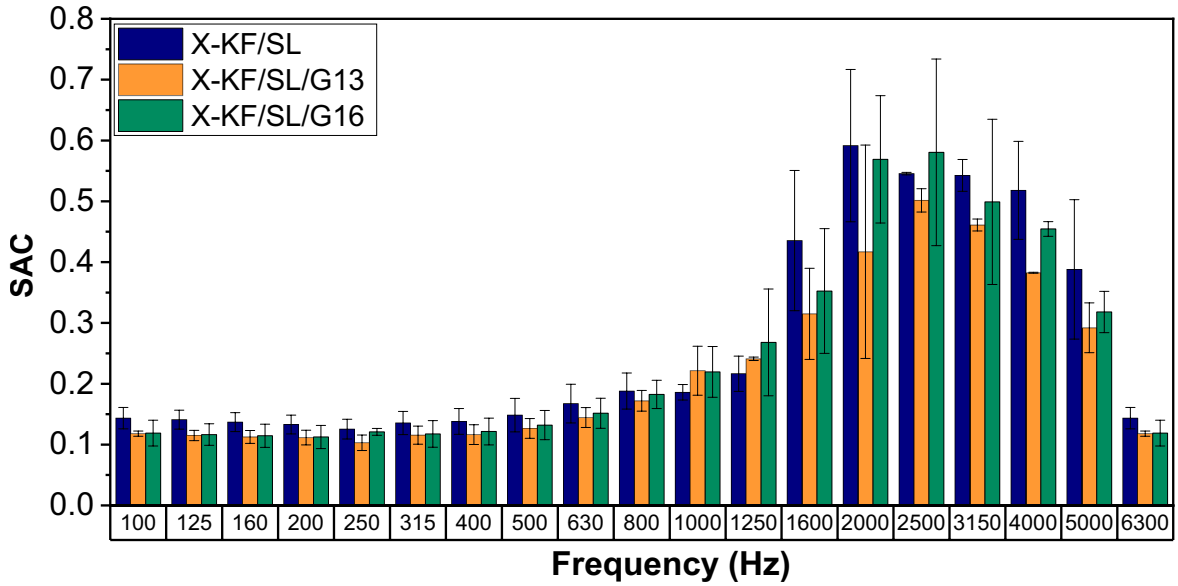

Fig. 10 Mean sound absorption coefficient (SAC) values measured in the frequency range of 100 Hz to 6300 Hz at intervals of 1/3 octaves for X-KF/SL, X-KF/SL/G13 and X-KF/SL/G16 xerogels

Table 7 Surface (ρ_S) and volume (ρ_V) resistivity of X-KF/SL, X-KF/G13, and biocomposites reinforced with natural fibers (Arumugam et al. 2021)[(a)], (Srinivasan et al. 2023)[(b)] (Gelfuso et al. 2011)[(c)] for comparison

Sample	Electrical resistivity behavior	
	Surface resistivity (ρ_S, Ω/square)	Volume resistivity (ρ_V, Ω cm)
X-KF/SL	4.75×10^{8}	1.13×10^{9}
X-KF/SL/G13	3.79×10^{8}	8.84×10^{8}
Saw dust/poly(C-a/DGEBA/ipda)[(a)]	6.49×10^{9}	7.51×10^{9}
Dessert cotton/poly(DGEBA-ipda)[(a)]	5.15×10^{8}	4.89×10^{8}
Areca nut husk/ poly(DGEBA-ipda)[(b)]	2.14×10^{9}	1.39×10^{9}
20% coconut fiber/80% polypropylene[(c)]	-	3.00×10^{9}

known for its electrical conductivity, within the material may impart dissipative properties to the electrically insulating polymer, consequently reducing electrical resistance (de Souza Vieira et al. 2021).

Focke and Mhike (2013) demonstrated that low-density polyethylene/graphite rotomolded composites, containing 5 wt% flake graphite, with a diameter of 112 µm, presented ρ_S ranging from 10^9 to 10^{10} Ω/square; at 10 wt% of graphite loading, the ρ_S value was reduced to 10^5 Ω/square, equal to the upper limit for conductive materials. For comparison, bio-composites containing saw dust (Arumugam et al. 2021), or desert cotton and areca nut husk (Srinivasan et al. 2023), were used to reinforce hybridized bio-benzoxazine/epoxy matrix. The resulting materials exhibited ρ_S and volume resistivity ρv values ranging from 10^8 to 10^9 Ω/square and Ω cm, respectively. Polypropylene matrix reinforced with mercerized coconut fibers showed an electrical resistivity of 3.0×10^9 Ω cm; the authors attributed the presence of ions on the fibers, which provided a path for the dissipation of electrostatic charges through the material (Gelfuso et al. 2011).

Conclusions

This study demonstrated that coating KFs with SL, an amphiphilic molecule, is a straightforward, fast, and cost-effective strategy to enhancing the fiber's hydrophilicity. This coating also facilitated interactions with G particles while preserving the original waxy layer on KF. The presence of SL's phosphatidyl and quaternary ammonium groups contributed to enhancing the thermal stability of the coated fibers. Moreover, SL helped dispersing both the fibers and G particles in aqueous solutions of HPMC. Regardless of the G content, the xerogels showed similar mechanical behavior and characteristics of elastomeric polymer foams under compression strain. The processing steps, along with the use of solvents (water and 70% v/v ethanol) were characterized by a low environmental impact. The synergistic combination of KF, SL, G, and HPMC yielded environmentally friendly materials with noteworthy mechanical, acoustic, and antistatic properties, rendering them potentially valuable for applications in packaging or building materials.

Author contributions All authors contributed to the study conception and design. Material preparation, data collection and analysis were performed by Daiana M. F. Sandrini, Olandir V. Correa, and Priyanka Madesh. The first draft of the manuscript was written by Daiana M.F. Sandrini and all authors commented on previous versions of the manuscript. Conceptualization, supervision, resources, funding acquisition, writing, review, and editing were performed by Denise F. S. Petri. All authors read and approved the final manuscript.

Funding D.M.F.S. is grateful for a CAPES fellowship (Proc. 88887.580710/2020-00). Finance Code 001. D.F.S.P. is grateful for grant support from FAPESP (grant 2018/13492–2) and Conselho Nacional de Desenvolvimento Científico e Tecnológico (CNPq Project No. 304017/2021).

Data availability No datasets were generated or analysed during the current study.

Declarations

Conflict of interest The authors have no relevant financial or non-financial interests to disclose.

References

Abdullah M, Shah NAFNMA, Saadun MAAM, Kadiran KA, Zaiton SN, Azman HA, Othman ZS, Osman MS (2019)

Comparative study of acid-treated and alkali-treated carbonised kapok-fibres for oil/water absorption system. J Phys Conf Ser 1349:012104. https://doi.org/10.1088/1742-6596/1349/1/012104

Albuquerque RQ, Meuchelböck J, Ruckdäschel H (2023) A unified approach for evaluating mechanical compression tests for polymer bead foams. J Polymer Sci 62(6):1034. https://doi.org/10.1002/pol.20230704

Alharby HF, Nahar K, Al-Zahrani HS, Hakeem KR, Hasanuzzaman M (2021) Enhancing salt tolerance in soybean by exogenous boron: intrinsic study of the ascorbate-glutathione and glyoxalase pathways. Plants. https://doi.org/10.3390/plants10102085

Arumugam H, Krishnasamy B, Perumal G, Anto Dilip A, Aleem MIA, Muthukaruppan A (2021) Bio-composites of rice husk and saw dust reinforced bio-benzoxazine/epoxy hybridized matrices: thermal, mechanical, electrical resistance and acoustic absorption properties. Constr Building Mater 312:125381. https://doi.org/10.1016/j.conbuildmat.2021.125381

Azevedo ALM, Oliveira RS, Ponzio EA, Semaan FS (2015) Sensor development exploiting graphite-epoxy composite as electrode material. IOP Conf Ser Mater Sci Eng. https://doi.org/10.1088/1757-899X/97/1/012008

Chen Y, Yin Z, Tang X (2022) Fabrication of sound absorption gypsum/hempcrete composite with robust antistatic electricity by Taguchi optimization method. J Nat Fibers 19:15891–15901. https://doi.org/10.1080/15440478.2022.2135668

Cluff DRA, Esmaeilli S (2009) Compressive properties of a new metal-polymer hybrid material. J Mater Sci 44:3867–3876

de Paula S, Holz S, Souza DHG, Pascholati SF (2021) Potential of resistance inducers for soybean rust management. Can J Plant Pathol 43:S298–S307. https://doi.org/10.1080/07060661.2021.1977999

de Souza VL, dos Anjos EGR, Verginio GEA (2021) Carbon-based materials as antistatic agents for the production of antistatic packaging: a review. J Mater Sci Mater Electron 32:3929–3947. https://doi.org/10.1007/s10854-020-05178-6

Dhanunjayarao B, Sanivada UK, Swamy Naidu N, Fangueiro R (2021) Effect of graphite particulate on mechanical characterization of hybrid polymer composites. J Ind Text. https://doi.org/10.1177/15280837211010670

Draman SFS, Daik R, Latif FA, El-Sheikh SM (2014) Characterization and thermal decomposition kinetics of kapok (*Ceiba pentandra* L.)-based cellulose. BioResources 9:8–23. https://doi.org/10.15376/biores.9.1.8-23

Fischgold H, Chain E (1934) The spontaneous decomposition of lecithin and its bearing on the determination of the isoelectric point. Biochem J 28:2044–2051. https://doi.org/10.1042/bj0282044

French AD (2014) Idealized powder diffraction patterns for cellulose polymorphs. Cellulose 21:885–896. https://doi.org/10.1007/s10570-013-0030-4

Futalan CM, Choi AES, Soriano HGO, Cabacungan MKB, Millare JC (2022) Modification strategies of kapok fiber composites and its application in the adsorption of heavy metal ions and dyes from aqueous solutions: a systematic review. Int J Environ Res Public Health 19:2703. https://doi.org/10.3390/ijerph19052703

GelfusoI MV, da Silva PVG, Thomazini D (2011) Polypropylene matrix composites reinforced with coconut fibers. Mater Res 14(3):360–365. https://doi.org/10.1590/S1516-14392011005000056

Hame D B, Scarlata C, Sluiter A (2008) Determination of protein content in biomass: laboratory analytical procedure (LAP); Issue Date 05/23/2008

Hashmi SAR, Dwivedi UK, Chand N (2007) Graphite modified cotton fibre reinforced polyester composites under sliding wear conditions. Wear 262:1426–1432. https://doi.org/10.1016/j.wear.2007.01.014

Hori K, Flavier ME, Kuga S et al (2000) Excellent oil absorbent kapok [*Ceiba pentandra* (L.) Gaertn.] fiber: fiber structure, chemical characteristics, and application. J Wood Sci 46:401–404. https://doi.org/10.1007/BF00776404

Hu S, Wang H, Wang F, Li Z, Bai J (2020) Synthesis of kappa fiber modified graphite carbon nitride with outstanding photocatalytic phenol degradation ability. Diam Relat Mater 105:107817. https://doi.org/10.1016/j.diamond.2020.107817

Kim SH, Heo Y-J, Park M, Min B-G, Rhee KY, Park S-J (2018) Effect of hydrophilic graphite flake on thermal conductivity and fracture toughness of basalt fibers/epoxy composites. Compos Part B Eng 153:9–16. https://doi.org/10.1016/j.compositesb.2018.07.022

Lee IH (2013) Use of lecithin as an antistatic agent in non-conductive crystallization slurries for isolating pure active pharmaceutical ingredients. Org Process Res Dev 17:1330–1334. https://doi.org/10.1021/op4001065

Li ZQ, Lu CJ, Xia ZP et al (2007) X-ray diffraction patterns of graphite and turbostratic carbon. Carbon N Y 45:1686–1695. https://doi.org/10.1016/j.carbon.2007.03.038

Liu X, Yan X, Li L, Zhang H (2015) Sound-absorption properties of kapok fiber nonwoven fabrics at low frequency. J Nat Fibers 12:311–322. https://doi.org/10.1080/15440478.2014.919891

Lyu L, Tian Y, Lu J, Xiong X, Guo J (2020) Flame-retardant and sound-absorption properties of composites based on kapok fiber. Materials 13:2845. https://doi.org/10.3390/ma13122845

Maceda A, Terrazas T (2022) Fluorescence microscopy methods for the analysis and characterization of lignin. Polymers 14:1–18. https://doi.org/10.3390/polym14050961

Mahmood T, Saddique MT, Naeem A et al (2011) Comparison of different methods for the point of zero charge determination of NiO. Ind Eng Chem Res 50:10017–10023. https://doi.org/10.1021/ie200271d

Marani PL, Bloisi GD, Petri DFS (2015) Hydroxypropylmethyl cellulose films crosslinked with citric acid for control release of nicotine. Cellulose 22:3907–3918. https://doi.org/10.1007/s10570-015-0757-1

Merino D, Ollier R, Lanfranconi M, Alvarez V (2016) Preparation and characterization of soy lecithin-modified bentonites. Appl Clay Sci 128:17–22. https://doi.org/10.1016/j.clay.2016.04.0060169-1317

Michał W, Ewa D, Tomasz C (2015) Lecithin-based wet chemical precipitation of hydroxyapatite nanoparticles. Colloid

Polym Sci 293:1561–1568. https://doi.org/10.1007/s00396-015-3557-0
Mishra T, Mandal P, Kumar A, Sahoo D (2022) A state-of-the-art review on potential applications of natural fiber-reinforced polymer composite filled with inorganic nanoparticle. Composites Part C Open Access A 9:100298. https://doi.org/10.1016/j.jcomc.2022.100298
Monteiro SN, Calado V, Margem FM, Rodriguez RJS (2012) Thermogravimetric stability behavior of less common lignocellulosic fibers—a review. J Mater Res Technol 1:189–199. https://doi.org/10.1016/S2238-7854(12)70032-7
Oladele IO, Oladejo MO, Adediran AA, Makinde-Isola BA, Owa AF, Akinlabi ET (2020) Influence of designated properties on the characteristics of dombeya buettneri fiber/graphite hybrid reinforced polypropylene composites. Sci Rep 10:11105. https://doi.org/10.1038/s41598-020-68033-y
Praba Karana C, Rengasamy RS, Das D (2011) Oil spill cleanup by structured fibre assembly. Indian J Fibre Text Res 36:190–200
Purnawati R, Febrianto F, Wistara INJ, Nikmatin S, Hidayat W, Lee SH, Kim NH (2018) Physical and chemical properties of kapok (*Ceiba pentandra*) and balsa (*Ochroma pyramidale*) fibers. J Korean Wood Sci Techn 46(4):393–401
Rao S, Jayaraman K, Bhattacharyya D (2011) Short fibre reinforced cores and their sandwich panels: processing and evaluation. Compos Part A Appl Sci Manuf 42:1236–1246. https://doi.org/10.1016/j.compositesa.2011.05.006
Rashid B, Leman Z, Jawaid M et al (2016) Physicochemical and thermal properties of lignocellulosic fiber from sugar palm fibers: effect of treatment. Cellulose 23:2905–2916. https://doi.org/10.1007/s10570-016-1005-z
Rezaei S, Pakdehi SG, Fathollahi M (2022) Conductivity enhancement and chargeability reduction of tetralin via some nonionic surfactants. J Electrostat 115:103677. https://doi.org/10.1016/j.elstat.2022.103677
Robinson N (1960) A light-scattering study of lecithin. Trans Faraday Soc 56:1260–1264. https://doi.org/10.1039/tf9605601260
Sartika D, Syamsu K, Warsiki E, Fahma F (2020) Isolation of microfiber cellulose from kapok fiber (*Ceiba pentandra*) by using chemical-hydrothermal treatment. Ecol Environ Conserv 26:654–662
Scholfield CR (1981) Composition of soybean lecithin. J Am Oil Chem Soc 58:889–892. https://doi.org/10.1007/BF02659652
Segal L, Creely JJ, Martin AE, Conrad CM (1959) An empirical method for estimating the degree of crystallinity of native cellulose using the X-ray diffractometer. Text Res J 29:786–794. https://doi.org/10.1177/004051755902901003
Shah PR, Gaitonde UN, Ganesh A (2018) Influence of soy-lecithin as bio-additive with straight vegetable oil on CI engine characteristics. Renew Energy 115:685–696. https://doi.org/10.1016/j.renene.2017.09.013
Silverstein RM, Webster FX, Kiemle DJ, Bryce DL (2014) Spectrometric identification of organic compounds, 8th edn. Wiley, Hoboken
Sluiter A, Hames B, Ruiz R, Scarlata C, Sluiter J, Templeton D (2011) Determination of structural carbohydrates and lignin in biomass. Lab Anal Proced (LAP) 1617:1–6
Smole M, Hribernik S, Stana K, Kree T (2013) Plant fibres for textile and technical applications. Adv Agrophysical Res. https://doi.org/10.5772/52372
Spinacé MAS, Lambert CS, Fermoselli KKG, De Paoli MA (2009) Characterization of lignocellulosic curaua fibres. Carbohydr Polym 77:47–53. https://doi.org/10.1016/j.carbpol.2008.12.005
Srinivasan H, Arumugam H, Dilip AA, Krishnasamy B, Aleem AMI, Murugesan A, Muthukaruppan A (2023) Desert cotton and areca nut husk fibre reinforced hybridized bio-benzoxazine/epoxy bio-composites: thermal, electrical and acoustic insulation applications. Constr Building Mater 363:129870. https://doi.org/10.1016/j.conbuildmat.2022.129870
Su S, Gao Y, Zhou X, Xiong X, Wang Y, Lyu L (2022) Structure of waste hemp stalks and their sound absorbing properties. Polymers 14:4844. https://doi.org/10.3390/polym14224844
Tao Z, Yang M, Wu L et al (2021) Phase change material based on polypyrrole/Fe_3O_4—functionalized hollow kapok fiber aerogel matrix for solar/magnetic-thermal energy conversion and storage. Chem Eng J 423(423):130180. https://doi.org/10.1016/j.cej.2021.130180
Veerakumar A, Selvakumar N (2012) A preliminar investigation on kapok/polypropylene nonwoven composite for sound absorption. Indian J Fiber Text Res 37:385–388
Wang R, Shin C-H, Park S, Park J-S, Kim D, Cui L, Ryu M (2014) Removal of lead (II) from aqueous stream by chemically enhanced kapok fiber adsorption. Environ Earth Sci 72:5221–5227. https://doi.org/10.1007/s12665-014-3804-6
Wang F, Zheng Y, Zhu Y, Wang A (2016) Oriented functionalization of natural hollow kapok fiber for highly efficient removal of toxic Hg(II) from aqueous solution. Front Environ Sci. https://doi.org/10.3389/fenvs.2016.00004
Wolok E, Lahay IH, Machmoed BR, Pakaya F (2019) Modification and characterization of *Ceiba pentandra* (L.) Gaertn. (Kapok) fiber: physical properties. Int J Res Granthaalayah 7:381–390. https://doi.org/10.29121/granthaalayah.v7.i7.2019.791
Xiang HF, Wang D, Liua HC et al (2013) Investigation on sound absorption properties of kapok fibers. Chin J Polymer Sci 31:521–529. https://doi.org/10.1007/s10118-013-1241-8
Yao F, Wu Q, Lei Y et al (2008) Thermal decomposition kinetics of natural fibers: activation energy with dynamic thermogravimetric analysis. Polymer Degrad Stab 93:90–98. https://doi.org/10.1016/j.polymdegradstab.2007.10.012
Zhang J-F, Tang R-C (2023) Preparation of phosphorylated kapok fiber using ammonium dihydrogen phosphate and its thermal degradation and fame retardancy. Cellulose 30:10733–10748. https://doi.org/10.1007/s10570-023-05552-7
Zhang X, Fu W, Duan C, Xiao H, Shi M, Zhao N, Xu J (2013) Superhydrophobicity determines the buoyancy performance of kapok fiber aggregates. Appl Surf Sci 266:225–229. https://doi.org/10.1016/j.apsusc.2012.11.153
Zhang J, Chang P, Zhang C, Xiong G, Luo H, Zhu Y, Ren K, Yao F, Wan Y (2015) Immobilization of lecithin on bacterial cellulose nanofibers for improved biological

functions. React Funct Polym 91–92:100–107. https://doi.org/10.1016/j.reactfunctpolym.2015.05.001

Zhang M, Zhang L, Tian S, Zhang X, Guo J, Guan X, Xu P (2020) Effects of graphite particles/Fe^{3+} on the properties of anoxic activated sludge. Chemosphere 253:126638. https://doi.org/10.1016/j.chemosphere.2020.126638

Zhang D, Zhou X, Gao Y, Lyu L (2022) Structural characteristics and sound absorption properties of waste hemp fiber. Coatings 12:1907. https://doi.org/10.3390/coatings12121907

Zheng Y, Wang J, Zhu Y, Wang A (2014) Research and application of kapok fiber as an absorbing material: a mini review. J Environ Sci 27:21–32. https://doi.org/10.1016/j.jes.2014.09.026

Zheng Y, Wang A (2014) Kapok fiber: applications. In: Hakeem KR et al (eds) Biomass and bioenergy. Springer International Publishing Switzerland, Cham, pp 251–256. https://doi.org/10.1007/978-3-319-07578-5_13

Zhou Y, Ning L, Li X (2015) Effect of natural flake graphite on triboelectrification electrostatic potential of bamboo flour/high-density polyethylene composites. Wood Sci Technol 49:1269–1280. https://doi.org/10.1007/s00226-015-0752-6